Biogeochemical fingerprinting of magnetotactic bacterial magnetite

Alberto Pérez-Huerta[a,b,1], Chiara Cappelli[a] , Ylenia Jabalera[c] , Tanya Prozorov[d] , Concepcion Jimenez-Lopez[c] , and Dennis A. Bazylinski[e]

Biominerals are important archives of the presence of life and environmental processes in the geological record. However, ascribing a clear biogenic nature to minerals with nanometer-sized dimensions has proven challenging. Identifying hallmark features of biologically controlled mineralization is particularly important for the case of magnetite crystals, resembling those produced by magnetotactic bacteria (MTB), which have been used as evidence of early prokaryotic life on Earth and in meteorites. We show here that magnetite produced by MTB displays a clear coupled C–N signal that is absent in abiogenic and/or biomimetic (protein-mediated) nanometer-sized magnetite. We attribute the presence of this signal to intracrystalline organic components associated with proteins involved in magnetosome formation by MTB. These results demonstrate that we can assign a biogenic origin to nanometer-sized magnetite crystals, and potentially other biominerals of similar dimensions, using unique geochemical signatures directly measured at the nanoscale. This finding is significant for searching for the earliest presence of life in the Earth's geological record and prokaryotic life on other planets.

biomagnetite | bacteria | biogeochemistry | atom probe tomography | magnetofossils

Establishing a reliable biogenic origin of minerals and recording environmental processes and the presence of past life in terrestrial and even extraterrestrial habitats remains a challenging endeavor (1–3). Different biological signatures have been assigned to minerals, yet there is no consensus on the criteria for the identification of their biogenic origin, even within the same type of minerals (4, 5). For instance, the use of morphology as a biosignature is difficult as geological processes can result in abiogenic self-organized crystalline structures indistinguishable from biogenic ones (6, 7). Rather than relying on a single mineral characteristic alone (i.e., morphology), biosignatures are defined by a combination of morphometric parameters (size, size/shape, circularity, crystallinity, fractal dimension, and lacunarity) (7) and chemical attributes, such as specific isotopic values or the presence of trace elements (3). Biominerals are, however, ubiquitous in nature and represent direct evidence of biological processes and the presence of life in the geological record (8). Biominerals resulting from biologically controlled processes are distinctive by the presence of intracrystalline organics, remnant of mineral nucleation and growth mechanisms, even after alteration by geological processes (9). Yet detecting such organics, and even more their unequivocal chemical signature, is extremely difficult in the case of "fossilized" minerals. The difficulty increases when the mineral size decreases to the nanoscale, as the identification of organics and their chemical fingerprinting falls often at or below the resolution of routinely employed microscopy and spectroscopy techniques.

The case of magnetite crystals produced by magnetotactic bacteria (MTB) is an ideal example of nanometer-sized minerals formed by biologically controlled processes. Ascribing a biogenic nature for magnetosome-like magnetite particles is of great importance as these particles, referred to as magnetofossils, have been used as evidence for the past presence of microbial activity in the geological record of Earth (10–13) and even on Mars since the discovery of certain types of magnetite crystals in the meteorite ALH84001 (14–16). Thus, several criteria have been proposed to distinguish between nanometric crystals of magnetite produced by bacteria and those produced by geological processes. Previous studies have explored the use of crystallographic and chemical characteristics of either whole cells or purified magnetosomes (11, 15). Results from some early studies suggested that magnetite crystals within magnetosomes were structurally identical to abiogenic crystals and stoichiometric (pure Fe_3O_4) (11, 13). Among these approaches, an interesting one has been to investigate the rate and total concentration of foreign cations that were possibly incorporated in the crystal lattice of magnetite nanocrystals produced by MTB (17–21). Moreover, the isotopic fractionation of iron and oxygen by MTB during magnetite biomineralization has also been investigated as a possible biosignature (21, 22). Despite these previous efforts, and the relevance of the subject, currently used criteria to recognize a biological origin of magnetite

Significance

Establishing a reliable biogenic origin of nanometer-sized minerals remains a challenging endeavor. We show a way to directly distinguish the biogenic nature of magnetite nanocrystals biomineralized by magnetotactic bacteria (MTB). Magnetite synthesized by MTB can be distinguished from other forms of abiogenic or biomimetic magnetite by a unique C–N geochemical signature. Our approach, using magnetosome magnetite crystals as a model biomineral, is applicable to detecting the biogenic origin of nanometer-sized minerals, crucial for the future exploration of the presence of life in the Earth's geological record and in extraterrestrial materials.

nanocrystals have not been accepted by many researchers as strong evidence, leaving room for controversy and debate (21). Thus, the ideal approach would be to analyze a few isolated magnetite nanocrystals, independently of morphology and in the absence of bacteria and/or a specific environment, to directly detect a biogeochemical signature linked to biomineralization processes.

Here, we establish the presence of chemical elements associated with organic molecules within magnetite nanocrystals produced by one type of MTB. The presence of specific chemical elements from intracrystalline organics could represent a biosignature not just for bacterial magnetite (BM) but also for other nanocrystals of possible biological origin. Our hypothesis is that since the biomineralization of magnetite magnetosome crystals in MTB is mediated by specific proteins associated with the magnetosome membrane, as unequivocally shown in numerous studies (18–23), these proteins are likely to imprint the magnetite crystal with a measurable amount of C and N that is not present in abiogenic or biomimetic (single protein–mediated) magnetite nanocrystals. For the direct examination and characterization of these chemical elements, we employ a combination of atom probe tomography (APT) and secondary ion mass spectrometry (SIMS and nano-SIMS). The high spatial chemical resolution of APT is ideal for the nanoscale dimensions of magnetosome magnetite crystals (24–26), whereas SIMS provides a confirmation of APT results of the presence of key elements at the μm scale while ruling out potential sources of contamination (27–29).

Results

Isolated, purified magnetite crystals (40–80 nm in size) were extracted from magnetosomes produced by the magnetotactic bacterium *Magnetospirillum gryphiswaldense* strain MSR-1 (Fig. 1) (18). These samples were compared to four different control samples (Fig. 1; see *Materials and Methods* and *SI Appendix*): 1) abiogenic magnetite nanocrystals, 2) abiogenic magnetite samples that underwent a washing protocol identical to that used to extract

and purify the magnetosomes, 3) biomimetic magnetite nanoparticles (BMNPs) chemically produced by including in the reaction mixture MamC from *Magnetococcus marinus*, and 4) abiogenic magnetite crystals included in a phosphatidylcholine liposome (L-MNPs). For the atom probe analysis of magnetosome and abiogenic particles, a focused ion beam (FIB) protocol for sample preparation was performed on a thin layer of cohesive crystals (*SI Appendix*, Fig. S1). A challenging aspect of APT analysis of this material is the presence of numerous voids among particles that are clear in the scanning electron microscopy images of the wedges and tips (*SI Appendix*, Fig. S1). For magnetosome particles, eight tips were extracted and three resulted in data (> 4.5 million reconstructed ions) for further analysis (*SI Appendix*, Table S1), including 3-dimensional (3D) tip reconstructions. APT results yielded significant compositional information of MTB magnetite through the identification and quantification of unique peaks in the mass spectra (Fig. 2 and *SI Appendix*, Table S2). APT bulk chemistry results showed relatively high concentrations of carbon present in MTB magnetite crystals that were not found in the rest of the control samples (Fig. 2 and Table 1 and *SI Appendix*, Table S1). The analysis of magnetosome particles showed the presence of C, corresponding to single peaks of C^+ (12 and 13 Da) and C^{2+} (6 and 6.5 Da) (Fig. 2C). Although there was variability among the three best-analyzed tips, all samples had a significant amount of C with an average ∼10 atomic % in concentration (Table 1 and *SI Appendix*, Table S2). The presence of C detected by APT in magnetosome magnetite was corroborated with SIMS analyses. The layer of crystals sampled for APT analysis was probed using SIMS (see *Materials and Methods* and *SI Appendix*, Fig. S6). Although absolute measurements were difficult to obtain, including $^{13}C/^{12}C$ ratios, because of the absence of magnetite standards with carbon, the counts for the ratio $^{12}C/^{56}Fe$ showed two orders of magnitude higher carbon content in magnetosome particles than in control samples (Table 1). APT also detected a measurable N concentration (∼0. 5 atomic %; *SI Appendix*, Table S2), corresponding primarily to N^+ (14 Da) and N^{2+} (7 Da) peaks in the APT mass spectra
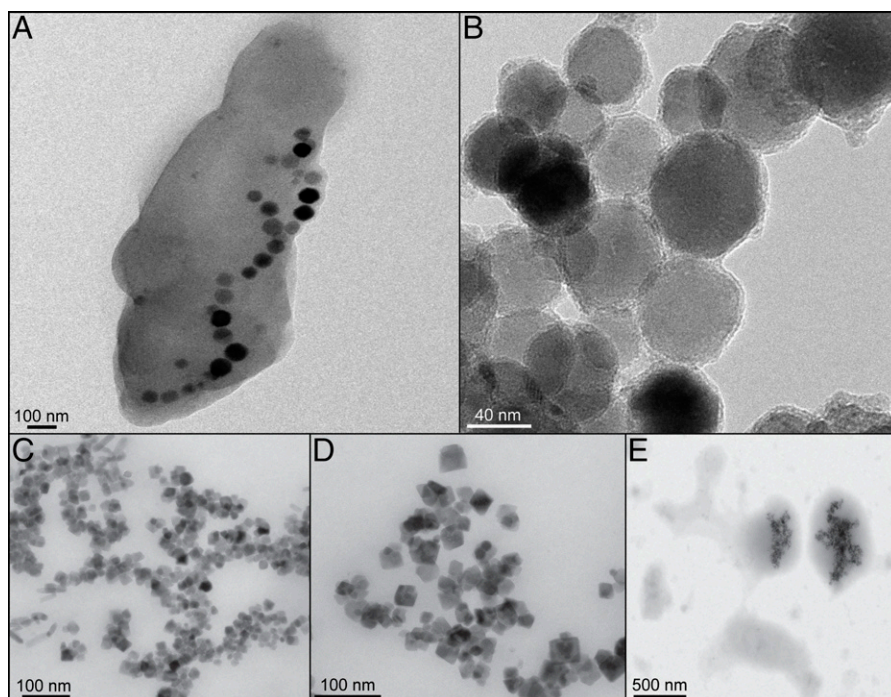

Fig. 1. Bright-field TEM images of analyzed samples. (*A*) Whole cell of magnetotactic bacterium *M. gryphiswaldense* MSR-1, with magnetite crystals inside. (*B*) Isolated magnetosome magnetite nanoparticles. (*C*) IM nanoparticles. (*D*) BMNPs, synthesized by adding MamC to IM. (*E*) L-MNPs.
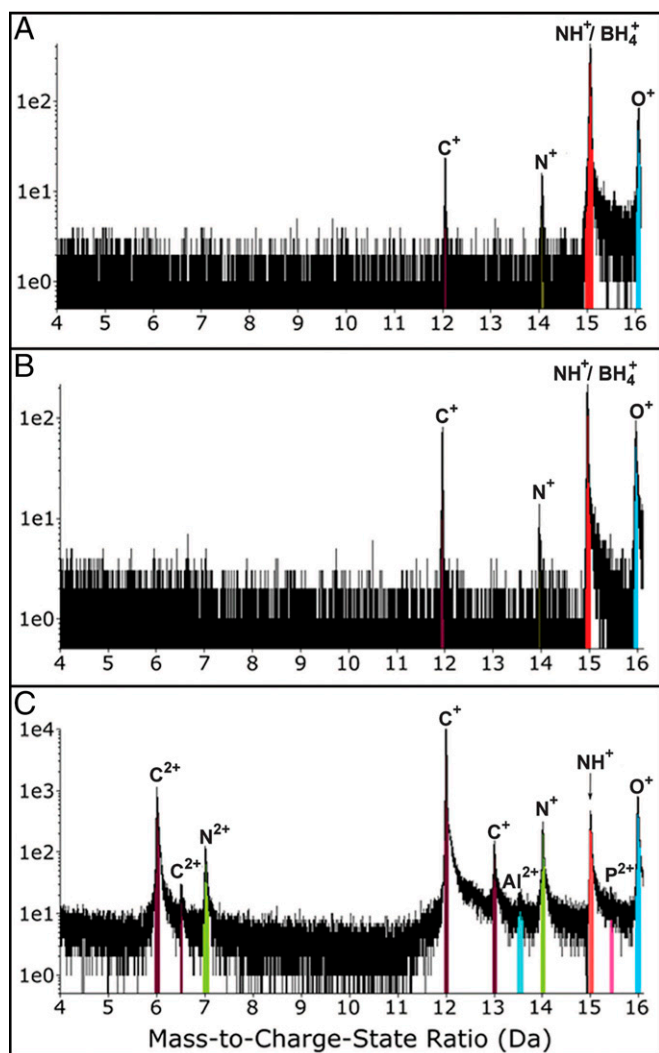
Fig. 2. Comparison of partial (from 4 Da to 16 Da) APT mass-to-charge state ratio spectra for (*A*) IM nanoparticles (sample 1.1; run 2775 in *SI Appendix*, Table S1), (*B*) IM-SDS nanoparticles (sample 2.1; run 3480 in *SI Appendix*, Table S1), and (*C*) BM (sample MSR-1; run 513 in *SI Appendix*, Table S1). Note the presence of specific C and N peaks in BM that are absent in abiogenic magnetite nanoparticles.

(Fig. 2*C*) in magnetosome magnetite, yet the concentration was low for the SIMS detection at µm scale (*SI Appendix*, Table S3).

The presence of C and N signals in BM was reinforced by their unique distribution inside the crystals, as observed in 3D tip reconstructions (Fig. 3). Taking the FeO atomic distribution as the marker for magnetite, the C was visible within the magnetite crystal with a nonuniform distribution. Isosurfaces of C concentration, at a C atomic % equivalent to that measured

Table 1. Comparison of average C composition from APT (atomic %) and SIMS (counts ^{12}C/^{56}Fe) analyses of BM, IM, and IM-SDS samples

	APT Carbon Data (atomic %)	SEM	SIMS Carbon Data (counts ^{12}C/^{56}Fe)	SEM
BM	10.94	1.28	803	1.34
IM	0.04	0.01	4.53	1.31
IM-SDS	0.21	0.08	6.3	1.17

See also *SI Appendix*, Tables S2 and S4 for data on other control samples.

for each tip, showed the presence of interconnected layers (Fig. 3 and *SI Appendix*, Fig. S3), which was different than any known artifacts resulting from APT tip reconstructions (26). Moreover, nitrogen distribution was found to be associated with that of carbon inside the magnetite particles, shown in 3D reconstructions as isolated areas of higher concentration inside the C layers (Fig. 3 and *SI Appendix*, Fig. S3).

Discussion

Evaluation of potential sources of contamination. Potential sources of contamination, specifically for C, must be ruled out to ascertain the reliable presence of C and N signals in magnetosome magnetite nanocrystals. The protocol for APT sample preparation may lead to the introduction of exogenous C. The porous structure of the magnetite multicrystal surface (the crust) could facilitate the implantation of C from the gas injection system platinum deposition during FIB sample preparation (see *SI Appendix*, Fig. S1). In such a case, we would have expected to see a uniform C concentration for all samples examined in this study, which is not what we observed for APT analyses of BM (see Table 1 and *SI Appendix*, Table S2). Within this context, it is important to notice that the SIMS data, which were not biased by the FIB preparation, showed that bacteria-produced crystals were enriched in C, in agreement with APT results (Table 1 and *SI Appendix*, Table S3). Furthermore, 3D reconstructions of the C distribution in magnetosome particles clearly showed the C inside the magnetite as opposed to the presence of C linked to contamination (Fig. 3).

Contamination derived from the protocol of magnetosome isolation and purification also needs to be addressed. Tris-HCl and SDS were used to remove the magnetosome membranes and extract the magnetosomes (see *SI Appendix*), thus potentially adding C-containing compounds. In this context, abiogenic (organic-free) magnetite crystals were produced (Fig. 1 and Table 1 and *SI Appendix*) and separated into two batches; one batch was kept untreated (IM; see Table 1 and *SI Appendix*, Table S1) and the second was treated with Tris-HCl and SDS (IM-SDS; see Table 1 and *SI Appendix*, Table S1) following an identical procedure to that used for the purification of magnetosomes. APT analyses of these abiogenic magnetite nanoparticles were compared to APT results from the MTB magnetosome magnetite crystals (*SI Appendix*, Table S2). The comparison revealed that C, but only as C$^+$ (12 Da), was detected in synthesized abiogenic magnetite nanoparticles (Fig. 2 and Table 1 and *SI Appendix*, Table S2). However, the concentration was extremely low and at least one order of magnitude lower than that measured for BM; these results were also confirmed by SIMS measurements (*SI Appendix*, Tables S1–S3). The evaluation of potential N contamination was more challenging and could only be done partially with the APT data. The reason is related to the signal contribution to peaks at 14 Da and 15 Da that could be attributed to either Si^{2+} and BH$_4^+$, possibly released by glass bottles where abiogenic magnetite crystals were synthesized, or to N$^+$ and NH$^+$ coming from the local electrode atom probe (LEAP) buffer chamber (30) (Fig. 2 and *SI Appendix*, Table S2). However, BM presented a peak at 7 Da that could only be attributed to N^{2+} (Fig. 2), and the concentration of N was much higher than that potentially attributed to silica and/or chamber contamination (*SI Appendix*, Table S2). Moreover, 3D APT tip reconstructions showed the presence of N strongly linked to that of C inside the magnetite crystals (Fig. 3 and *SI Appendix*, Fig. S3). This observation also ruled out the possibility of organics diffusing into the magnetite
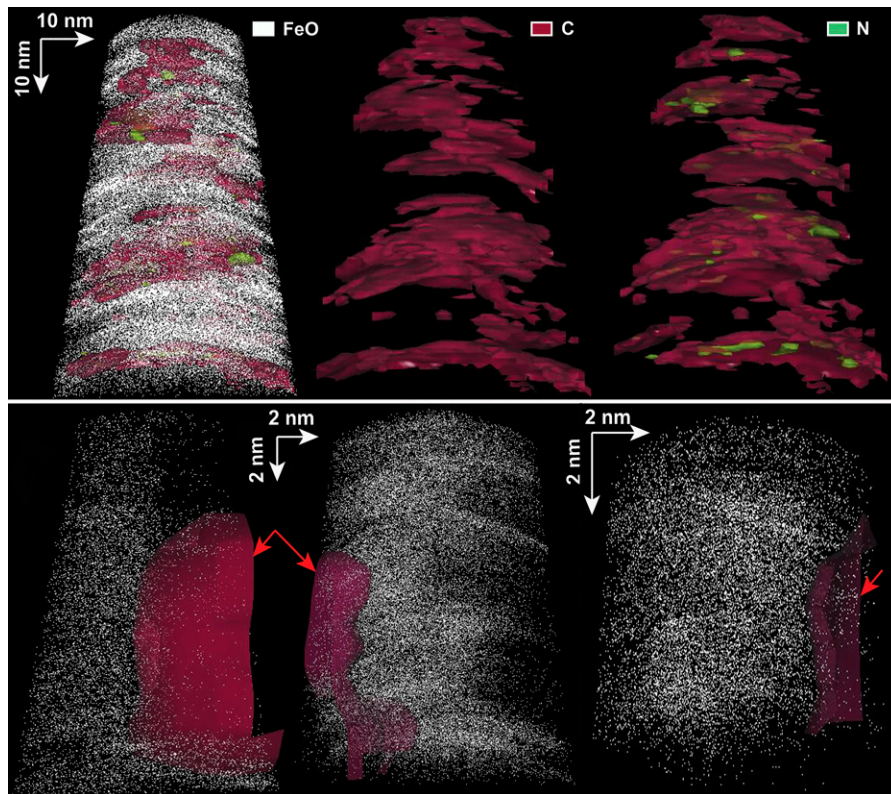
Fig. 3. Comparison of APT 3D reconstructions of bacterial magnetite (tip 514) (*Top*) and control samples (*Bottom*) for IM-SDS (*Left*; tip 3480), BMNPs (*Middle*; tip 3468), and L-MNPs (*Right*; tip 3733) (see also *SI Appendix*, Tables S1, S2, and S4). For the BM, note the presence of C and N (occupying spaces inside C layers), reconstructed as isosurfaces at the same atomic % as that measured for these elements in these specific tips (see *SI Appendix*, Table S1), inside magnetite (represented by the FeO distribution). For the control samples, C resulting from contamination (red arrows) is not inside the magnetite but is rather found on the outside of the tips.

crystals after their formation, unless such organics were present during precipitation (31).

C and N in magnetosome magnetite. The detected C–N signal found in the BM could be the result of residues of the magnetosome membrane tightly bonded to the surface of crystals, even though a harsh protocol was applied for its removal (see *SI Appendix*). Morphological features resembling membrane residues were not observed by scanning electron microscopy at a high spatial resolution (~20 nm) on the magnetite crust and around particles prior to and during APT sample preparation (*SI Appendix*, Fig. S1). In addition, membrane fragments on the surface of biomagnetite crystals should be captured by the APT data, yet we only saw the coupled C–N signal inside the crystals in the 3D reconstructions (Fig. 3). To further confirm the absence of membrane fragments on the surface of the magnetosome magnetite particle layer, we conducted a surface analysis using nano-SIMS adjacent to the area where APT and SIMS analyses were performed. If membrane residues were present, then we would expect to see a prevalent phosphorus signal, with phosphorus even detected at low counts (see *SI Appendix*, Fig. S7), linked to the phospholipid nature of the membrane, and this was not the case (see *SI Appendix*, Fig. S7). As an additional test, we synthesized magnetite nanoparticles contained in phosphatidylcholine liposomes (L-MNPs) (32) (Fig. 1 and *SI Appendix*, Table S4). The rationale behind this approach was to estimate the maximum C signal that could be associated with the membrane if the organic chemical signal detected in the magnetosomes was the result of membrane residues. The APT chemical estimate, using the peaks at 6 and 12 Da as representative of C, clearly indicated that C represented only averages ~3 atomic % for L-MNPS

nanoparticles, quite below the minimum (~8 atomic %) detected in BM nanoparticles (Table 1 and *SI Appendix*, Tables S2 and S4). However, most of this C was attributed to contamination based on APT 3D reconstructions (Fig. 3), so the ~3 atomic % measured could represent an overestimate. This hypothesis was confirmed because the SIMS data showed that C was not a significant component on the surface of L-MNPs particles (see *SI Appendix*, Table S3). Overall, these results reaffirmed that the C signal detected in magnetosome magnetite particles is not significantly derived from magnetosome membrane residues.

Our hypothesis was that the C–N signature is related to intracrystalline organic components incorporated within the magnetite crystal lattice and as such can be used as a biomineral signature. This hypothesis is supported by SIMS analysis of BMNPs, synthesized in the laboratory by the mediation of the protein MamC from *M. marinus*, that have been suggested to incorporate or at least to have MamC strongly attached to the magnetite crystal (33). SIMS data indicated that the C signal is higher for BMNPs than other synthesized particles, which could be in part attributed to proteins (*SI Appendix*, Table S3). Bulk APT carbon data (Fig. 3 and *SI Appendix*, Table S4) did not show a significant increase of the C signal associated to BMNPs, as only few and part of the particles are analyzed in a single tip. In addition, BMNPs were made with a low concentration of a single protein, whereas magnetosome particles would have the contribution of several proteins involved in mineral formation, so in the latter case a more uniform distribution of organics would be expected. This would explain the strong detection and colocation of C and N in the 3D APT reconstructions of tips extracted from the magnetosome magnetite crystals (see Fig. 3 and *SI Appendix*, Fig. S3). On the other

hand, APT 3D analysis of tips composed of abiogenic nanoparticles exposed to organics from the SDS treatment (IM-SDS) or the liposome (L-MNPs) did not show the incorporation of C or N inside the magnetite crystals (Fig. 3). These observations, in combination with the APT and SIMS bulk chemical data, support our hypothesis that the C–N signature is likely the result of the incorporation of part- or whole-magnetosome proteins, such as Mms6 and MamC, and it could be an explanation for variations in lattice parameters previously reported in magnetosome magnetite crystals (34). These proteins have been shown to control the nucleation and growth of magnetite in vitro, and the incorporation of the protein or amino acid residues in the growing crystal has been suggested and/or indirectly evidenced (35–39). However, APT cannot provide an absolute quantification of the amount of protein inside the magnetite crystals because ion loss, especially for elements with lower masses, is known to occur in the analysis of biominerals (25, 40). This prevents making more precise estimates of chemical element ratios (i.e., C–N) and identifying the contributions of specific magnetosome proteins.

In conclusion, we present evidence that a coupled C–N signal, likely linked to intracrystalline organic matter from proteins, is unique to BM crystals. The presence of the C signature is further confirmed by SIMS analysis. This is in great contrast to laboratory-synthesized magnetite nanocrystals used as examples of abiogenic magnetite nanometer-sized particles to rule out contamination in our analysis of magnetosome crystals. The presence of a newly established biogeochemical fingerprinting of magnetosome magnetite has significant implications for the use of nanometer-sized magnetite crystals as potential magnetofossils. The chemical signal of intracrystalline organics can be preserved in magnetofossils, while the magnetite crystal structure is not degraded. Magnetite in sediments can be altered during diagenesis because of the oxidation of magnetite to maghemite (with the same spinel ferrite structure as magnetite) and/or dissolution of the magnetite crystal by the H_2S generated by the anaerobic respiration of sulfate-reducing bacteria (41). Therefore, magnetosomes preserved from oxygen and anaerobic sediments rich in SO_4^{2-} would be less prone to being altered (42). Furthermore, magnetite in ancient geological deposits is usually preserved, and isolated from microorganisms, in silicate- or iron-rich rock layers (13, 42, 43) or by other mineral phases in extraterrestrial samples (4, 41). In addition, the high spatial-chemical resolution of combining APT and nano-SIMS is ideal for probing the biogenic origin of isolated magnetite crystals from bacteria, in contrast to previous chemical approaches requiring large quantities of crystals and/or knowledge about bacteria and environmental parameters (19, 21, 22), recently found magnetite nanocrystals in other organisms (44), and the nanometer- to µm-sized magnetofossils (13). Finally, our approach, using magnetosome magnetite crystals as a model biomineral, is applicable to detecting the biogenic origin of other nanometer-sized minerals crucial for exploring the presence of life in the Earth's geological record and in extraterrestrial materials.

Materials and Methods

Samples. For a comprehensive understanding of the biogeochemical fingerprinting of BM, we compared magnetosome magnetite samples to a suite of synthesized magnetite nanoparticles (Fig. 1). Samples used in this study, with a detailed sample preparation methodology in *SI Appendix*, are described as follows: 1) BM–magnetite nanoparticles were obtained from magnetosomes precipitated by *M. gryphiswaldense* MSR-1 (18); 2) magnetite nanoparticles–inorganically synthesized magnetite nanoparticles, resembling those produced

by the bacteria, were used to evaluate potential sources of C–N contamination during sample preparation and magnetosome membrane removal. Two set of samples, one with untreated particles (IM) and another washed with SDS (IM-SDS), were produced. To understand the biological origin of the C and N signal recorded in BM, we compared magnetosome magnetite particles to BMNPs and magnetoliposomes (L-MNPs).

Scanning transmission electron microscopy and transmission electron microscopy. Details of the transmission electron microscopy (TEM) characterization of BM nanoparticles, including additional images, can be found in Prozorov et al. (18). For the characterization of synthesized nanoparticles, further details and images can be found in Jabalera et al. (31).

FIB work. The preparation of APT tips of BM nanoparticles was conducted at The University of Alabama in Tuscaloosa, whereas the preparation of APT tips of synthesized nanoparticles was carried out at the Ames National Laboratory (Ames, IA). APT tips were fabricated by FIB in dual-beam scanning electron microscopy, a TESCAN LYRA XMU housed at the Alabama Analytical Research Center (AARC) of The University of Alabama, and an FEI Helios NanoLab G3 Ultimate Characterization at the Ames National Laboratory, respectively, by adapting a well-established FIB-based lift-out protocol (24,45). Specific details of sample preparation with the two scanning electron microscopy instruments can be found in *SI Appendix*.

LEAP work and data analysis. BM samples and the synthesized magnetite nanoparticle samples were analyzed with a LEAP 5000 XS equipped with a picosecond 355 nm ultraviolet laser from CAMECA Instruments, housed at the AARC. Representative analysis conditions for the BM and abiogenic magnetite samples (IM and IM-SDS) can be found in *SI Appendix*, Table S1 (the same running parameters were used for samples of BMNPs and L-MNPs).

The data were reconstructed using Integrated Visualization and Analysis Software (IVAS, version 3.8.8) from CAMECA Instruments. Peak ranges were defined as the entire visible peak or were adjusted manually when large thermal tails were present. The reconstructions were completed by fitting the time-of-flight mass spectrum iteratively using the voltage and bowl-fitting parameters within the IVAS platform (*SI Appendix*, Figs. S5 and S6). The 3D reconstructions of APT data for BM (Fig. 3 and *SI Appendix*, Fig. S3) and one tip of the control samples of IM-SDS, BMNPs, and L-MNPs (Fig. 3), as representative of C atomic distribution from contamination, were performed using the "shank" tip profile method. For all nanoparticles, the shank methodology had to be used because the ionization of nanoparticles produced numerous voltage outbursts during runs.

SIMS and nano-SIMS. Both SIMS and nano-SIMS analysis was conducted at the NSF Multiuser Facility of Arizona State University.

SIMS (*SI Appendix*, Fig. S7): The sample surfaces used to extract the tips for APT analysis, from samples of BM, IM, IM-SDS, BMNPs, and L-MNPs, were analyzed with SIMS after plasma cleaning of the surface. Analyses were done using a CAMECA SIMS 6f instrument (MRP 3,300; Ip = 5 nA; 75 µm image field; fourth field aperture). Initially, exploratory measurements were made with a 30 µm spot size and final data were collected using a 4 µm spot size (*SI Appendix*, Fig. S7). Counts were collected for 12C, 16O, 12C14N, 31P, 32S, and 56Fe, and ratios are reported for 12C/56Fe and 12C/12C14N using the average of 3 analyses per sample (*SI Appendix*, Table S3).

Nano-SIMS (*SI Appendix*, Fig. S8): For the magnetosome magnetite sample, a region adjacent to where APT and SIMS analyses were conducted, a high-resolution map (25*25 µm, 256*256 pixels, 5 ms/pixel dwell time, and 30 planes), after adding 20 sift-corrected images, was carried out using a CAMECA Nano-SIMS 50 L and a 25 nm Cs+ beam (*SI Appendix*, Table S3).

Data Availability. All data related to the manuscript, including samples and aspects of methodology, are included in the main manuscript or as part of *SI Appendix*. Requests for additional data (i.e., APT data files), details of protocols, materials, and for any questions related to the manuscript, should be addressed to the corresponding author, Dr. Alberto Pérez-Huerta (aphuerta@ua.edu). Original IVAS files (RHIT and HITS) data are available in Figshare (45).

1. E. J. Javaux, Challenges in evidencing the earliest traces of life. *Nature* **572**, 451–460 (2019).
2. J. M. García-Ruiz, E. Nakouzi, E. Kotopoulou, L. Tamborrino, O. Steinbock, Biomimetic mineral self-organization from silica-rich spring waters. *Sci. Adv.* **3**, e1602285 (2017).
3. B. Cavalazzi *et al.*, Cellular remains in a ~3.42-billion-year-old subseafloor hydrothermal environment. *Sci. Adv.* **7**, 3963–3977 (2021).
4. K. L. Thomas-Keprta *et al.*, Elongated prismatic magnetite crystals in ALH84001 carbonate globules: Potential Martian magnetofossils. *Geochim. Cosmochim. Acta* **64**, 4049–4081 (2000).
5. D. C. Golden *et al.*, Evidence for exclusively inorganic formation of magnetite in Martian meteorite ALH84001. *Am. Mineral.* **89**, 681–695 (2004).
6. J. M. García Ruiz, A. Carnerup, A. G. Christy, N. J. Welham, S. T. Hyde, Morphology: An ambiguous indicator of biogenicity. *Astrobiology* **2**, 353–369 (2002).
7. J. Rouillard *et al.*, Identifying microbial life in rocks: Insights from population morphometry. *Geobiology* **18**, 282–305 (2020).
8. H. H. A. Lowenstam, S. Weiner, *On Biomineralization* (Oxford University Press, 1989).
9. A. Pérez-Huerta, I. Coronado, T. A. Hegna, Understanding biomineralization in the fossil record. *Earth Sci. Rev.* **179**, 95–122 (2018).
10. R. E. Kopp, J. L. Kirschvink, The identification and biogeochemical interpretation of fossil magnetotactic bacteria. *Earth Sci. Rev.* **86**, 42–61 (2008).
11. J. Baumgartner *et al.*, Magnetotactic bacteria form magnetite from a phosphate-rich ferric hydroxide via nanometric ferric (oxyhydr)oxide intermediates. *Proc. Natl. Acad. Sci. U.S.A.* **110**, 14883–14888 (2013).
12. R. Uebe, D. Schüler, Magnetosome biogenesis in magnetotactic bacteria. *Nat. Rev. Microbiol.* **14**, 621–637 (2016).
13. S. B. R. Chang, J. L. Kirschvink, Magnetofossils, the magnetization of sediments, and the evolution of magnetite biomineralization. *Annu. Rev. Earth Planet. Sci.* **17**, 169–195 (1989).
14. D. S. McKay, Search for past life on Mars: Possible relic biogenic activity in martian meteorite ALH84001. *Science* **273**, 924–930 (1996).
15. K. L. Thomas-Keprta *et al.*, Truncated hexa-octahedral magnetite crystals in ALH84001: Presumptive biosignatures. *Proc. Natl. Acad. Sci. U.S.A.* **98**, 2164–2169 (2001).
16. K. L. Thomas-Keprta, S. J. Clemett, D. S. McKay, E. K. Gibson, S. J. Wentworth, Origins of magnetite nanocrystals in Martian meteorite ALH84001. *Geochim. Cosmochim. Acta* **73**, 6631–6677 (2009).
17. C. N. Keim, U. Lins, M. Farina, Manganese in biogenic magnetite crystals from magnetotactic bacteria. *FEMS Microbiol. Lett.* **292**, 250–253 (2009).
18. T. Prozorov *et al.*, Manganese incorporation into the magnetosome magnetite: Magnetic signature of doping. *Eur. J. Mineral.* **26**, 457–471 (2014).
19. M. Amor *et al.*, Chemical signature of magnetotactic bacteria. *Proc. Natl. Acad. Sci. U.S.A.* **112**, 1699–1703 (2015).
20. M. Tanaka *et al.*, Biomagnetic recovery and bioaccumulation of selenium granules in magnetotactic bacteria. *Appl. Environ. Microbiol.* **82**, 3886–3891 (2016).
21. M. Amor *et al.*, Mass-dependent and -independent signature of Fe isotopes in magnetotactic bacteria. *Science* **352**, 705–708 (2016).
22. K. W. Mandernack, D. A. Bazylinski, W. C. Shanks III, T. D. Bullen, Oxygen and iron isotope studies of magnetite produced by magnetotactic bacteria. *Science* **285**, 1892–1896 (1999).
23. H. Nudelman, R. Zarivach, Structure prediction of magnetosome-associated proteins. *Front. Microbiol.* **5**, 9 (2014).
24. L. M. Gordon, D. Joester, Nanoscale chemical tomography of buried organic-inorganic interfaces in the chiton tooth. *Nature* **469**, 194–197 (2011).
25. L. M. Gordon *et al.*, Dental materials. Amorphous intergranular phases control the properties of rodent tooth enamel. *Science* **347**, 746–750 (2015).
26. F. Vurpillot, A. Cerezo, D. Blavette, D. J. Larson, Modeling image distortions in 3DAP. *Microsc. Microanal.* **10**, 384–390 (2004).
27. E. A. Bell, P. Boehnke, T. M. Harrison, W. L. Mao, Potentially biogenic carbon preserved in a 4.1 billion-year-old zircon. *Proc. Natl. Acad. Sci. U.S.A.* **112**, 14518–14521 (2015).
28. N. Morag *et al.*, Microstructure-specific carbon isotopic signatures of organic matter from ~3.5 Ga cherts of the Pilbara Craton support a biologic origin. *Precambrian Res.* **275**, 429–449 (2016).
29. J. W. Schopf, K. Kitajima, M. J. Spicuzza, A. B. Kudryavtsev, J. W. Valley, SIMS analyses of the oldest known assemblage of microfossils document their taxon-correlated carbon isotope compositions. *Proc. Natl. Acad. Sci. U.S.A.* **115**, 53–58 (2018).
30. D. Haley, I. McCarroll, P. A. J. Bagot, J. M. Cairney, M. P. Moody, A gas-phase reaction cell for modern atom probe systems. *Microsc. Microanal.* **25**, 410–417 (2019).
31. Y. Kuwahara, T. Miyazaki, Y. Shirosaki, M. Kawashita, Effects of organic polymer addition in magnetite synthesis on the crystalline structure. *RSC Advances* **4**, 23359–23363 (2014).
32. Y. Jabalera, A. Fernández-Vivas, G. R. Iglesias, Á. V. Delgado, C. Jimenez-Lopez, Magnetoliposomes of mixed biomimetic and inorganic magnetic nanoparticles as enhanced hyperthermia agents. *Colloids Surf. B Biointerfaces* **183**, 110435 (2019).
33. G. García Rubia *et al.*, pH-dependent adsorption release of doxorubicin on MamC-biomimetic magnetite nanoparticles. *Langmuir* **34**, 13713–13724 (2018).
34. A. Fischer, M. Schmitz, B. Aichmayer, P. Fratzl, D. Faivre, Structural purity of magnetite nanoparticles in magnetotactic bacteria. *J. R. Soc. Interface* **8**, 1011–1018 (2011).
35. A. Yamagishi *et al.*, Control of magnetite nanocrystal morphology in magnetotactic bacteria by regulation of *mms7* gene expression. *Sci. Rep.* **6**, 29785 (2016).
36. M. Tanaka, E. Mazuyama, A. Arakaki, T. Matsunaga, MMS6 protein regulates crystal morphology during nano-sized magnetite biomineralization in vivo. *J. Biol. Chem.* **286**, 6386–6392 (2011).
37. A. Arakaki *et al.*, Comparative subcellular localization analysis of magnetosome proteins reveals a unique localization behavior of Mms6 protein onto magnetite crystals. *J. Bacteriol.* **198**, 2794–2802 (2016).
38. C. Valverde-Tercedor *et al.*, Size control of *in vitro* synthesized magnetite crystals by the MamC protein of *Magnetococcus marinus* strain MC-1. *Appl. Microbiol. Biotechnol.* **99**, 5109–5121 (2015).
39. H. Nudelman *et al.*, Structure-function studies of the magnetite-biomineralizing magnetosome-associated protein MamC. *J. Struct. Biol.* **194**, 244–252 (2016).
40. A. Pérez-Huerta, F. Laiginhas, Preliminary data on the nanoscale characterization of the inter-crystalline organic matrix of a calcium carbonate biomineral. *Minerals (Basel)* **8**, 223 (2018).
41. L. E. Hays *et al.*, Biosignature preservation and detection in Mars analog environments. *Astrobiology* **17**, 363–400 (2017).
42. M. Amor, F. P. Mathon, C. L. Monteil, V. Busigny, C. T. Lefevre, Iron-biomineralizing organelle in magnetotactic bacteria: Function, synthesis and preservation in ancient rock samples. *Environ. Microbiol.* **22**, 3611–3632 (2020).
43. B. Rasmussen, J. R. Muhling, B. Krapež, Greenalite and its role in the genesis of early Precambrian iron formations–A review. *Earth Sci. Rev.* **217**, 103613 (2017).
44. H. Yang *et al.*, Magnetic foraminifera thrive in the Mariana Trench. *Geochem. Perspect. Lett.* **21**, 23–27 (2022).
45. https://figshare.com/projects/Perez-Huerta_PNAS_Biomagnetite_APT_Files/143037